Customizing H 2 O-Poor Electric Double Layer and Boosting Texture Exposure of Zn (101) Plane towards Super-High Areal Capacity Zinc Metal Batteries

Yangyang Wang, Jiaxin Lv, Laixin Hong, Jiakai Zhang, Chunxia Chen, Ao Xu, Miao Huang, Xiubin Ren, Jinbo Bai, Hui Wang, et al.

Customizing H_2O-Poor Electric Double Layer and Boosting Texture Exposure of Zn (101) Plane towards Super-High Areal Capacity Zinc Metal Batteries

Yangyang Wang[1], Jiaxin Lv[1], Laixin Hong[1], Jiakai Zhang[1], Chunxia Chen[1], Ao Xu[1], Miao Huang[1], Xiubin Ren[3], Jinbo Bai[2], Hui Wang[1] and Xiaojie Liu[1]*

[1] *Key Laboratory of Synthetic and Natural Functional Molecule of the Ministry of Education, College of Chemistry & Materials Science, Northwest University, Xi'an 710127, P. R. China*

[2] *Laboratoire Mécanique des Sols, Structures et Matériaux (MSSMat), CNRS UMR 8579, Ecole CentraleSupélec, Université Paris-Saclay, 8-10 rue Joliot-Curie, 91190 Gif-sur-Yvette, France*

[3] *College of Chemistry and Chemical Engineering, Xi'an University of Science and Technology, Xi'an, 710054, P.R. China*

* Corresponding Author:

E-mail address: xiaojie.liu@nwu.edu.cn (X. Liu)

Abstract:

The catastrophic dendrite hyperplasia and parasitic reactions severely impede the future deployment of aqueous Zn-ion batteries. Controlling zinc orientation growth is considered to be an effective method to overcome the aforementioned concerns, especially for regulating the (002) plane of deposited Zn. Unfortunately, Zn (002) texture is difficult to obtain stable cycling under high deposition capacity resulting from its large lattice distortion and nonuniform distribution in electric field. Herein, different from traditional cognition, a crystallization orientation regulation tactic is proposed to boost Zn (101) texture exposure and inhibit zinc dendrite proliferation during plating/stripping. Experimental results and theoretical calculations demonstrate the malate molecules preferentially adsorb on the Zn (002) facet, leading to the texture exposure of distinctive Zn (101) plane. Meanwhile, the –COOH and –OH groups of malate molecules exhibit strong adsorption on the Zn anode surface and chelate with Zn^{2+}, achieving H_2O-poor electrical double layer. Very impressively, the multifunctional malate additive enlists zinc anode to survive for 600 h under a harsh condition of 15 mA cm^{-2}/15 mAh cm^{-2}. Moreover, the symmetric cell harvests highly-reversible cycling life of 6600 h at 5 mA cm^{-2}/1.25 mAh cm^{-2}, remarkably outperforming the $ZnSO_4$ electrolyte. The assembled Zn//MnO_2 full cells also demonstrate prominent electrochemical reversibility.

Keywords: preferential orientation, electrical double layer, multifunctional regulation, ultrahigh capacity, zinc anode

1.Introduction

Metallic zinc (Zn) has recently received significant attention as anode material in rechargeable aqueous Zn-ion batteries (AZIBs) for large-scale energy storage, thanks to its high theoretical capacity (820 mAh g^{-1} and 5855 mAh cm^{-3}), appropriate redox potential (–0.762 V vs standard hydrogen electrode (SHE)), outstanding safety and environmental benignity.[1] Nevertheless, the utilization of Zn metal anode suffers from uncontrolled Zn dendrite accumulation, and malignant water-induced side-reactions including competitive H_2 evolution reaction (HER) as well as unavoidable corrosion and passivation of electrode,[2] which eventually result in unsatisfactory electrochemical reversibility and inferior chemical stability during zinc plating/stripping processes, thus limiting their commercialization.[3] Hence, exploring simple and effective means to achieve zinc anodes with excellent reversibility/stability is crucial to development of AZIBs.

Thus far, various states-of-art tactics, including the use of 3D anode design,[4] surface coating,[5] and electrolyte additive[6] have been applied to suppress the dendrite formation and corrosion. Among them, a suitable electrolyte additive stands out because of its tractable and time-saving implementation process, and its ability to effectively ameliorate the stability of Zn anodes.[7] In general, the electrochemical reaction between the metal Zn anode and the electrolyte primarily occurs within the electrical double layer (EDL), which plays a critical role in determining the Zn^{2+} deposition process.[8] The classical EDL model comprises a Helmholtz plane (HP) and a diffusion layer (DL), where HP includes inner Helmholtz layer (IHL) and outer Helmholtz layer (OHL).[9] In a conventional aqueous system, solvated Zn^{2+} cations and H_2O molecules will enter the HP on the zinc anode side before the desolvation and deposition reaction of zinc ions during the first charge, leading to uneven distribution of EDL components between the zinc electrode and the electrolyte.[10] Typically, in $ZnSO_4$ electrolytes, the coordination H_2O in the $[Zn(H_2O)_6]^{2+}$ solvation sheath in traditional EDL receives electrons and intensifies H_2 precipitation during de-solvation and zinc electroplating process, which can lead to an increase in OH^-

concentration and the formation of zinc hydroxide byproducts with the participation of Zn^{2+}, SO_4^{2-} and H_2O.[11] In response to the above issue, seeking for suitable electrolyte additive is crucial to modulate the electrode/electrolyte interface environment, particularly customizing a H_2O-poor EDL to improve anodic stability towards advanced AZIBs. Meanwhile, the effect of the EDL regulation through an electrolyte addition strategy on suppressing side reactions towards aqueous zinc-ion batteries is still mysterious and needs to be unraveled.

In addition to hydrogen evolution and corrosion of zinc, dendrite proliferation is a prevalent issue resulting in the failure of cells due to short-circuit. Recent studies have highlighted that the crystal orientation has a significant influence on the morphology of zinc deposits.[12] As we all know, the (002)-orientated zinc plating has been extensively realized by electrolyte-guided deposition, mainly due to its numerous advantages including low surface energy, low HER activity, strong ability against corrosion and planar deposition.[13] However, the higher chemical stability of the Zn (002) facet basically means lower chemical activity and sluggish crystal growth tendency, thus necessitating relatively larger polarization to drive zinc stripping in the battery.[14] In addition, Zn deposited on the texture (002) substrate is likely to deviate from the original lattice growth arising from the weak bonding of Zn (002) upon deposited atoms, give rising in the accumulation of lattice distortion. Consequently, (002) zinc deposition is unable to maintain continuous epitaxy, limiting the ability to effectively manage deposited Zn under a higher planting capacity.[15] Recently, Zhang et al. have demonstrated that the Zn (101) facet with higher surface energy and stronger epitaxy effect achieves ordered growth, thereby displaying exceptional Zn deposition kinetics.[15] Meanwhile, the Zn (101) plane is considered to be a highly reactive plane, and its rapid ion reaction kinetics are more dominant than the Zn (002) facet in term of the competitive reaction with H^+/H_2, leading to the inhibition of side reactions, delivering an excellent CE and cycling lifespan.[16] Therefore, tuning the states of the plated zinc crystal along the (101) direction promises to fundamentally achieve highly reversible and stable zinc metal anodes through the use of an appropriate electrolyte additive. Unfortunately, so far the multifunctional regulation

mechanism of electrolyte additive affecting Zn electrodeposition with preferential orientation of the unconventional (101) crystal plane, in relation with areal capacity, have not been fully and systematically investigated. More importantly, the correlation between the established H_2O-poor EDL and Zn preferential orientation of (101) plane is still unclear and needs to be clarified. No such work has been conducted. As far as we know, apple acid, also known as malate, is a type of organic acid that is commonly used as an acidulant and flavor enhancer in the food and beverage industries. Meanwhile, the structure of malate consists of two carboxylic acid groups, making it a dicarboxylic acid. This structure exhibits the ability to provide multiple coordination sites for metal ions, a crucial characteristic in its application as an electrolyte additive of AZIBs.[17] In addition, malate is a non-toxic and environmentally friendly compound, which is a desirable feature for electrolyte additives. Therefore, it is highly expected that the abundance of polar functional groups (–COOH, –OH) and high electron density in malate molecules can affect the Zn striping/plating behavior.

Herein, a preferential exposure of unconventional Zn (101) facet is demonstrated to be extremely effective in promoting dendrite-free zinc deposition by adopting a small amount of malate (Mal) molecules as an electrolyte additive. Experimental results and theoretical calculations reveal that due to the presence of abundant polar groups (–COOH, –OH), malate molecules exhibit strong adsorption ability on Zn anode surface, resulting in a thicker H_2O-poor EDL and improved suppression effects of corrosion (Figure 1a). Besides, the adsorbed malate hinders the Zn^{2+} deposition along the (101) direction and benefits the zinc ions diffuse along the (100) and (002) direction, achieving the preferred Zn (101) plane orientation exposure. Benefiting from this unconventional texture exposure pattern, the assembled Zn//Zn symmetrical cell yields an ultra-long lifespan for more than 6600 h at 5 mA cm^{-2}/1.25 mAh cm^{-2}, which can still operate stably over 600 h at both ultrahigh current density of 15 mA cm^{-2} and areal capacity of 15 mAh cm^{-2}. The Zn//Cu cell harvests an exceptional cycling life with a high CE of 99.5% over 6000 cycles at 5 mA cm^{-2}/1 mAh cm^{-2}. Moreover, the long-term cycling performance of full cells based on MnO_2 and I_2@CF cathodes can be effectively enhanced. To further explore the practical application

value for its commercialization, the cells with Gel/SA-Mal are also successfully assembled and deliver superior cyclability.

2.Results and Discussion

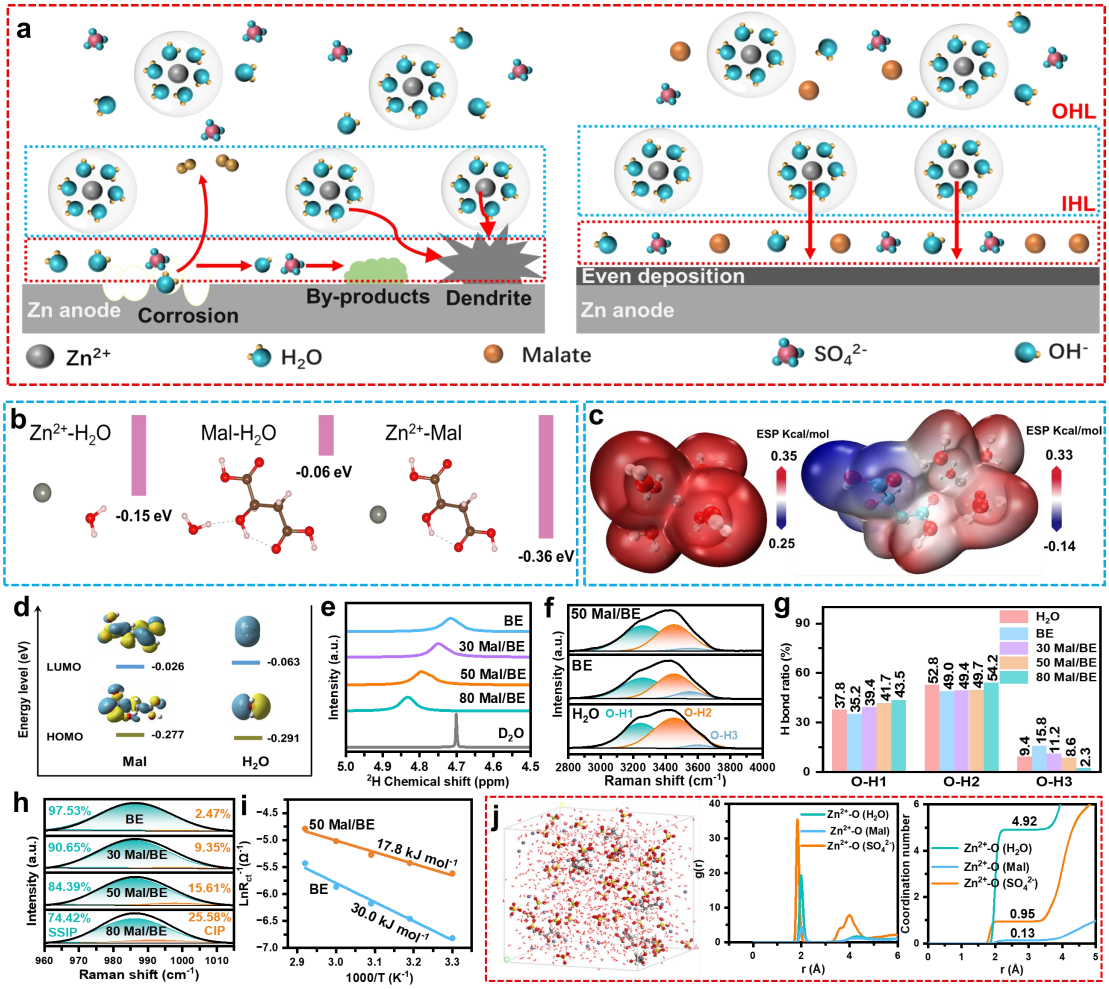

Figure 1. Physiochemical property of malate additive and solvation structure. (a) Schematic diagrams for Zn deposition cycled in BE and Mal/BE. (b) DFT calculated binding energies of Zn^{2+} in association with different compounds (malate and H_2O). (c) Electrostatic potential mapping of the original Zn^{2+}-$6H_2O$ in comparison to Zn^{2+}-$5H_2O$-malate. (d) Isoelectronic density surfaces for the LUMO and HOMO of malate (left) and H_2O molecules (right). (e) ^2H NMR spectra of different compound solutions. (f) Raman spectra of H_2O, BE, and the 50 Mal/BE, and (g) summary of the correlations of the H-bonds ratio. (h) Raman spectra for composite solutions, distinguishing the two solvent structures: SSIP and CIP. (i) The calculated de-solvation activation energies (E_a) of Zn//Zn symmetrical cells with BE and 50 Mal/BE at different temperatures. (j) 3D snapshots of $ZnSO_4$-H_2O-Mal obtained from MD simulations and the radial distribution functions and coordination number of Zn^{2+}-O collected from MD simulations in $ZnSO_4$-H_2O-Mal.

2.1. Preparation and Properties of Electrolytes

Inspired by its widespread application in the food industry, malate (Mal) molecules could be also utilized as a electrolytes additive of battery to facilitate aqueous zinc chemistry based on the following consideration. A 2 M $ZnSO_4$ solution has been considered as the base electrolyte (BE), and different electrolytes by adding 30, 50, and 80 mM malate to the BE are studied. These samples are denoted as 30 Mal/BE, 50 Mal/BE, and 80 Mal/BE, respectively. According to the electrostatic potential (ESP) mapping (Figure S1a, Supporting Information), the –COOH and –OH site of malate molecules exhibit electronegativity, suggesting that this site is easily bound by cations and undergoes electrophilic reactions. Malate molecules is highly soluble in H_2O (Figure S1b, Supporting Information), and the prepared electrolytes remains uniformly dissolved with no significant changes for 1 month, indicating the compatibility and continued solvation of malate in the $ZnSO_4$ environment. Besides, Mal/BE reflects high thermal stability, maintaining its performance even when exposed to temperatures as high as 60°C for 120 h (Figure S1c, Supporting Information). This outstanding thermal stability facilitates its application as an additive in the $ZnSO_4$ electrolyte, guaranteeing its stable operation even under higher temperatures. Moreover, the stability of zinc anode in the electrolyte is affected by the value of pH, and co-evolution of H_2 tends to occur in a lower pH environment. As shown in Figure S2, Supporting Information, a slight decrease in pH value after the addition of malate is acquired, which can be ascribed to the –COOH group in malate. Hence, the harm caused by the reduction of pH is negligible due to the use of small amounts of malate.

2.2. The Reconstruction of HP in the EDL Structure by Malate Additive

The influence of malate molecules on the solvation structure of Zn^{2+} ions is firstly studied adopting density functional theory (DFT) calculations. Notably, the binding energy (Figure 1b) of Zn^{2+}-Mal (−0.36 eV) is found to be higher than Zn^{2+}-H_2O (−0.15 eV) and Mal-H_2O (−0.06 eV), indicating that Zn^{2+} ions are more inclined to associate with Mal molecules than H_2O inside the solvent sheath. For an intuitive comparison, the Bader charge analysis is performed for three structures (Figure S3, Supporting Information). The electron donation from zinc to malate is 0.08 e, higher

than that from zinc to H_2O (0.07 e). Meanwhile, H_2O also interacts with malate, as evidenced by the binding energy and the electron donation (0.04 e). This result means that the enrichment of malate molecules on the zinc anode surface to generate H_2O-poor interface within the HP, which could stop H_2O molecules from contacting the zinc anode with mitigated corrosion reaction.[18] The difference in EDL capacitance in BE and 50 Mal/BE also supports this adsorption behavior, as EDL capacitance can be regarded as a practical parameter for assessing the state of interface between electrode and electrolyte.[19] Clearly, as presented in Figure S4, Supporting Information, the capacitance of 50 Mal/BE (56.11 μF cm^{-2}) is significantly lower than that of BE (84.56 μF cm^{-2}) calculated from the equation： $i_c=C\nu$ (Equation S1, Supporting Information).[20] The diminished capacitance measured by alternating current (AC) voltammetry should reasonably be attributed to the effect of the competitive adsorption behavior of the double-charged malate molecules that enter HP and line up on the zinc surface, rather than the H_2O molecules (Figure S5, Supporting Information).[21] The preferred adsorption of malate molecules rather than H_2O on zinc anode can be further confirmed by molecular energy levels (Figure 1d). Specifically, the malate molecules show a reduced lowest occupied molecular orbital (LUMO) and an elevated highest occupied molecular orbital (HOMO) position that of H_2O, reflecting that malate can easily acquire electrons and will be reduced to the solid electrolyte interphase (SEI) ahead of H_2O, thus inhibiting the side reaction on the zinc anode surface and therefore forming fewer byproducts. When one H_2O molecule is replaced by one molecule of malate in the Zn^{2+}-$6H_2O$, the electrostatic potential value significantly decreases (Figure 1c). This reduction implies a mitigation in electrostatic repulsion around Zn^{2+} ions, which is beneficial to rapid transportation of cations. To effectively demonstrate the SEI formation, X-ray photoelectron spectroscopy (XPS) is utilized to examine the composition of the *in situ* formed SEI. With the increase of sputtering depth, the intensity of C=O peak shows a clear tendency to stabilize (Figures S6a,b, Supporting Information). Additionally, sulfate signals can be detected in the O 1s spectra (Figure S6b, Supporting Information), likely due to the precipitation of zinc salts in the $ZnSO_4$ electrolyte. It is of particular

interest to note that the high-resolution S 2p spectra not only verify the presence of SO_4^{2-} (79.4%) but also signify the presence of ZnS species (20.6%) (Figure S6c, Supporting Information). Concurrently, as the sputtering depth increases, the content of SO_4^{2-} diminishes to 48.0%, while ZnS species content rises to 45.8%. Also, a minor presence of SO_3^{2-} species (6.2%) is detected, indicating the development of a ZnS-rich solid electrolyte interphase. In the case of zinc metal deposited in the $ZnSO_4$ electrolyte, only the SO_4^{2-} characteristic peak is evident in the S 2p spectra. This observation implies that the SO_3^{2-} and ZnS components may arise from the reduction of SO_4^{2-} by hydrogen gas produced during the electrochemical reaction between malate and Zn in the initial cycles. Based on previous reports, ZnS is crucial for enhancing the stability and reversibility of zinc metal anodes.

2.3. The Effect of Malate Additive on Diffusion Layer of the EDL Structure

During zinc plating process, malate molecules is adsorbed on the electrolyte/electrode interface to reshape the characteristics of HP. It is possible that malate molecules interact with SO_4^{2-} ions and active H_2O molecules, causing them to insert into the primary solvation sheath (PSS) of Zn^{2+} ions, and altering the PSS balance of Zn^{2+} ions into the diffusion layer, which can be further experimentally demonstrated by the nuclear magnetic resonance (NMR), Raman spectroscopy, and Fourier transform infrared spectroscopy (FTIR) characterizations. As illustrated in Figure S7, Supporting Information, the NMR spectrum of ^1H nuclei reveals that the interaction between malate molecules and SO_4^{2-} ions. As the concentration of malate in the $ZnSO_4$ electrolyte increases, several peaks corresponding to malate encounters a notable shift toward the high field position resulting from the amplified surrounding electron density of hydrogen atoms. More solid evidence can be found in the deuterium (2H, D) NMR (Figure 1e), the ^2H peak of D_2O is typically observed at 4.702 ppm, while the peak shifts to a lower field for chemical shift values in BE, attesting a shielding effect caused by the deuterium nuclei in D_2O arising from the hydration effect of Zn^{2+} ions present in the electrolyte. When malate in BE increases from 30 mM to 80 mM, the ^2H peaks of D_2O move successively toward a higher chemical shift, which proves that the reduced activity of free water and the

establishment of robust hydrogen bond networks from the −OH groups of H_2O molecules and malate molecules. The diminished activity of H_2O in the Mal/BE is useful as it contributes to inhibit the undesired HER and alleviates the constraints imposed by anions on cations.

Raman spectra further demonstrate the effect of the malate additives on the hydrogen bond network and solvation structure of Zn^{2+}. In the Figures 1f,g and Figure S8, Supporting Information, O─H1, O─H2, and O─H3 stand for a robust hydrogen bond, medium a weaker hydrogen bond, and non-hydrogen bonding H_2O molecules, respectively.[22] Compared with pure H_2O, the peak area ascribing to O─H1 in BE shows a decreasing trend, which implies that some free-water molecules are involved in the formation of $[Zn(H_2O)_6]^{2+}$ complexes. On the other hand, the introduction of 30 mM malate into the BE results in an increased ratio in the O─H1, signifying that malate solvation releases a subset of H_2O molecules. What's more, the proportion of O─H2 and O─H3 components in the BE is higher than that in pure H_2O, indicating the H_2O molecules and the SO_4^{2-} ions around Zn^{2+} are involved in the hydrogen bonding interaction. After the introduction of malate into the BE, the proportions of O─H2 unit undergo a gradually augmented situation, evidencing a progressive expansion of the hydrogen bond networks. This tendency can be attributed to the –OH and –COOH functional groups of malate molecules acting as electron donors, developing a connection with hydrogen atoms from H_2O. As a result, the previously active H_2O molecules are no longer regarded as "free", and a substantial hydrogen bond network is established between malate and H_2O molecules in the Mal/BE. This expansion of hydrogen bond networks can be further evidenced by FTIR analysis (Figures S9a,b, Supporting Information). As the concentration increases for malate additive, significant red shifts and wider peaks are found in the bending vibration of –OH groups located at 3100–3800 cm^{-1}. These changes suggest an increased interaction between H_2O and malate molecules, causing the formation of stronger hydrogen bonds. In addition, a slight blue shift appears in the bending vibration of H_2O within the 1650–1700 cm^{-1} range, providing more evidence for improved hydrogen bonding among H_2O molecules. This shift means that malate molecules

occupy the active sites of H_2O in the solvation structure, resulting in the electrolyte environment recombination in the diffusion layer of EDL.

Beyond that, the hydrogen atoms in malate molecules can also accept lone pairs of electrons from the oxygen atoms in SO_4^{2-} ions, leading to the reconstruction of hydrogen bond networks. Raman spectroscopy is further employed to excavate the involvement of SO_4^{2-} ions in the solvation structure. In the $ZnSO_4$-based electrolyte, two forms of ion-pair species exist according to their association degree, namely solvent-separated ion pairs (SSIP, $[Zn^{2+}(H_2O)_6 \cdot SO_4^{2-}]$) and contact ion pairs (CIP, $[Zn^{2+}(H_2O)_5 \cdot OSO_3^{2-}]$), as displayed in Figure 1h. The broad peaks observed near 980 cm^{-1}, assigning to the vibrational stretching of the SO_4^{2-} (v-SO_4^{2-}) band in the presence of various concentrations of malate additives, are separated to determine the contributions from SSIP and CIP.[23] With the augment of malate content, the v-SO_4^{2-} band moves toward higher frequencies, and the percentage of CIP progressively increases. This observation signifies that the hydrogen bonds between malate and H_2O weaken the interaction between H_2O and Zn^{2+}, guaranteeing more SO_4^{2-} ions to enter into the primary solvation sheath. In addition, FTIR also reflects a weakening of the constraints around the SO_4^{2-} within Mal/BE (Figure S9c, Supporting Information). In the BE system, the v-SO_4^{2-} is observed at 1079.9 cm^{-1}, while a continuous blue shift in v-SO_4^{2-} is found when increasing malate concentration in the BE, manifesting that a weakened constraint around SO_4^{2-}.

It has been proven that the desolvation of Zn^{2+} is the critical obstacle to ion migration upon the zinc deposition process. [24] Hence, the desolvation ability of Zn^{2+} in both BE and 50 Mal/BE are quantitatively evaluated by determining the activation energy (E_a) based on the Arrhenius equation (Equation S2, Supporting Information).[25] As shown in Figure S10 and Table S1, Supporting Information, the R_{ct} of the symmetric cells including BE and 50 Mal/BE is acquired via electrochemical impedance spectroscopy (EIS) profiles at various temperatures (30–70°C). The cell using BE exhibits an E_a-value of 30.0 kJ mol^{-1}. In addition, the E_a-value of the cell with 50 Mal/BE decreases to 17.8 kJ mol^{-1}, meaning that the newly formed EDL is conducive to desolvation and ion transport processes (Figure 1i). Moreover, the

addition of malate notably promotes migration of Zn^{2+} ion in the electrolyte, as evident by the comparatively higher Zn^{2+} transference number (t_{Zn}^{2+}) in the 50 Mal/BE in contrast to BE (Figure S11 and Equation S3, Supporting Information). The above improvements evidence that the weakened Zn^{2+} solvation to guarantee rapid transport of Zn^{2+}, thereby endowing the process of zinc stripping/plating with competitive reaction kinetics.[26] Subsequently, molecular dynamics (MD) simulations are conducted to investigate the effects of malate additives on $ZnSO_4$ electrolyte . In the BE system, the results indicate that average one Zn^{2+} is coordinated with six H_2O molecules and one SO_4^{2-} anion. Meanwhile, the 3D snapshot shows that the coordination number of H_2O molecules in the Zn^{2+} primary solvation shell is replaced by introduced malate molecules. The coordination number (ACN) of solvated Zn^{2+} is applied by radial distribution functions (RDFs). For Mal/BE system, a sharp Zn–O (Mal) peak appears at around 2 Å in the distance, which is the same as that of BE, implying the insertion of the double charged malate into the PSS of Zn^{2+}. Moreover, the coordination number of H_2O molecules drops from 4.97 to 4.92, suggesting that malate tends to replace the inner water and penetrate the PSS of Zn^{2+} to coordinate with Zn^{2+} (Figure 1j and Figure S12, Supporting Information).[18] This ingress possesses potential to reduce the presence of active H_2O molecules, thus effectively lowering the occurrence of serious HER and its adverse by-reactions.

In short, based on the combination of above discussion, the positive roles of malate molecules in reshaping the EDL structure and chemistry can be attributed as follows. (i) The additive of malate molecules can not only adjust Zn^{2+} solvation structure with the formation of $[Zn(H_2O)_5(Mal)]^{2+}$ resulting from the interactions between malate and Zn^{2+} ions, provide a 3D transport channel for Zn^{2+} ions, but also destroy original H-bonds networks to rebuild novel H-bonds. (ii) a H_2O-poor EDL on the zinc anode side can be customized through chemical attachment with Zn^{2+} ions, which can isolate H_2O as a corrosion inhibitor to corrode zinc anode surface, thus greatly facilitating stability and reversibility of zinc metal anode.

2.4. Suppression of Corrosion and Hydrogen Evolution by Malate Additive

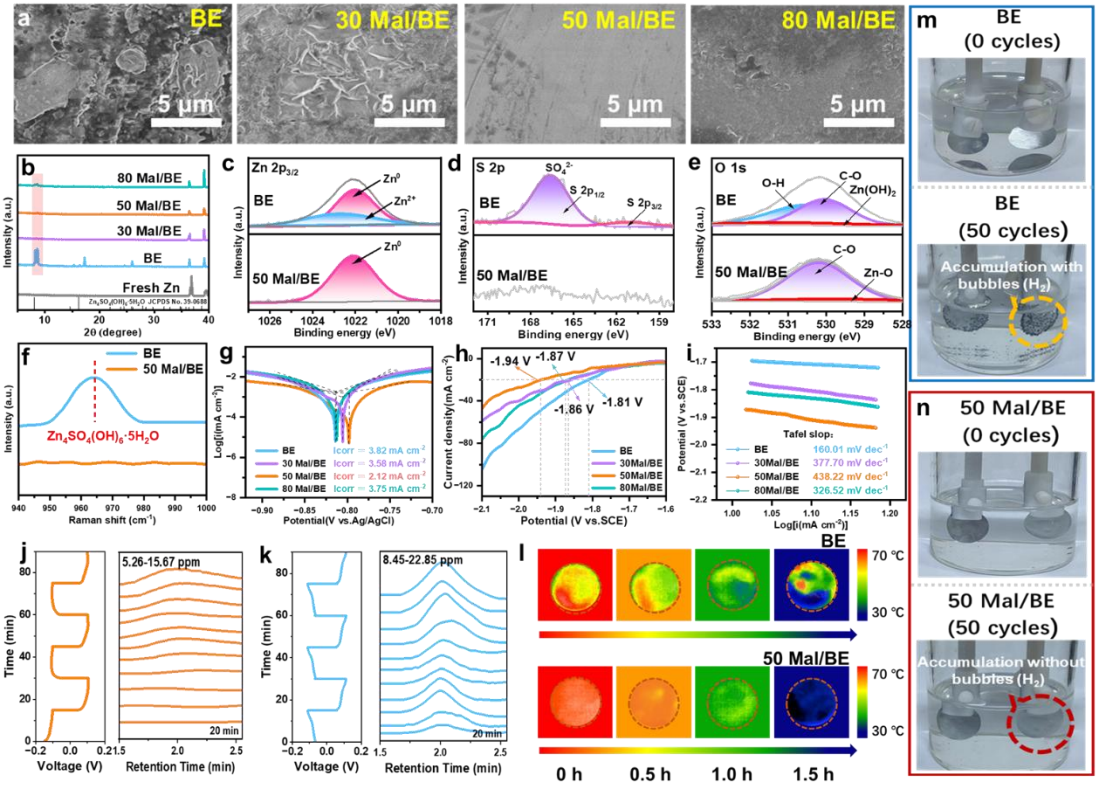

Figure 2. Side reaction resistance of Zn electrode without/with malate additive. (a) SEM images of Zn foils following 3-day immersion in BE, 30 Mal/BE, 50 Mal/BE, and 80 Mal/BE. (b) XRD patterns of the Zn soaked in different electrolytes. The XPS spectra of (c) Zn 2p, (d) S 2p, and (e) O 1s on the surface of Zn foil soaked in the BE and 50 Mal/BE. (f) Raman spectra of Zn soaked in the BE and 50 Mal/BE. (g) Tafel curves for describing corrosion of Zn anodes in different electrolytes. (h) Hydrogen evolution polarization curves and (i) corresponding Tafel plots of zinc anode in different solutions. Ex situ GC of AZIBs during stripping/plating process of (j) 50 Mal/BE and (k) BE system. (l) Infrared thermography images of Zn anode in BE and 50 Mal/BE after 50th plating. In situ optical microscopy observation of zinc deposition on zinc foils in (m) BE and (n) 50 Mal/BE after 50 cycles.

The potential of using malate additive to facilitate corrosion resistance of Zn anodes is investigated through immersion experiments. Following a 3-day immersion of Zn foil in the BE, a rugged surface morphology with a considerable number of hexagonal flake-like crystals is observed on the zinc anode surface from scanning electron microscopy (SEM) (Figure 2a). This phenomenon can be ascribed to vigorous side reactions and subsequent formation of corrosion by-products ($Zn_4SO_4(OH)_6 \cdot 5H_2O$), which can be demonstrated by X-ray diffraction (XRD) patterns with an emerging evident peak (Figure 2b). Upon introducing different

concentrations of malate (30, 50, and 80 mM) to the electrolyte, a relatively flat and uniform surface is maintained (Figure 2a). Besides, as respectively displayed by the 3D optical microscopy images in Figure S13, Supporting Information, the Zn electrode in 50 Mal/BE possess a flat surface with a small height R_a of 44.2 nm, while that in the BE show significant undulations in height ($R_a \approx 64.1$ nm), implying the effective dendrite inhibition ability of malate molecules. Additionally, the absence of the by-products peak in the Raman spectrum is also evidence that malate could effectively inhibit $Zn_4SO_4(OH)_6 \cdot 5H_2O$ production (Figure 2f). This situation is also characterized by XPS spectra for the electrode after soaking (Figures 2c–e). The results manifest that there is a significant improvement in anti-corrosion performance after the addition of malate by chemisorbing onto zinc surface via –OH and –COOH functional groups. The discrepancy in corrosion among these electrolytes is closely linked to the adsorption capability of malate additive on zinc surface. To assess the adsorption capabilities, variations in contact angle are measured for different electrolytes (Figure S14, Supporting Information). The contact angle between BE and Zn foil is recorded as 98°. The introducing of different concentrations of malate (30, 50, and 80 mM) into BE leads to the decease of contact angles to 76°, 57° and 48°, respectively, indicating that the presence of –OH and –COOH groups are beneficial for the wettability of aqueous electrolytes. This chemisorption effect can be confirmed through the FTIR analysis. FTIR result display evident peaks located at 1140 cm^{-1}, assigning to the C─O stretching vibration of malate on the zinc foil immersed in 50 Mal/BE (Figure S15, Supporting Information).[27] Additionally, the EIS test is conducted to investigate ionic conductivity of both BE and Mal/BE (Figure S16 and Equation S4, Supporting Information), demonstrating a noticeable improvement in ionic conductivities of Mal/BE in contrast to BE. Furthermore, infrared thermal imaging is applied to verify formation and distribution of by-products by leveraging the difference in thermal conductivity of Zn anode and $Zn_4SO_4(OH)_6 \cdot 5H_2O$. Figure 2l clearly reveals that Zn anode possesses uniform thermal distribution in the cooling process under the presence of malate additive, indicating it has a homogenous surface.

In order to accurately measure suppression effect of HER reaction in Mal/BE

during Zn deposition/dissolution process, linear sweep voltammetry (LSV) test is investigated. For the HER activity test, the onset potential of the HER in the Mal/BE is higher compared to the BE, especially when the malate additive concentration is 50 mM (Figure 2h), revealing a reduction in the risk of H_2 generation due to electrolyte solvation structure. And the corresponding Tafel slope fitted by LSV profiles in Figure 2i reflect that the most remarkable damping of HER kinetics occurs with 50 Mal/BE, with a value of 438.22 mV dec^{-1}. This highlights significant efficacies of malate as an inhibitor in restraining the water decomposition reaction. As revealed in Tafel polarization profiles (Figure 2g and Figure S17, Supporting Information), the Mal/BE displays a lesser corrosion current density and a higher corrosion potential than BE, reflecting a well-restrained corrosion rate and tendency of Zn anodes with the presence of malate in aqueous electrolytes. Besides, the degree of interface HER reaction is a key factor in judging corrosion in zinc anode. To accurately quantify the inhibition of HER, ex-situ GC analysis is performed on zinc symmetric cells using both BE and 50 Mal/BE (Figures 2j,k). Evidently, when solution O_2 is removed, the 50 Mal/BE system shows a significant reduction in the amount of H_2 produced in contrast to BE systems. The concentration of H_2 in the 50 Mal/BE system ranges from 5.26 to 15.67 ppm, in sharp contrast to BE systems, displaying a range of 8.45 to 22.85 ppm. The H_2 generation originates from parasitic reactions occurring in the Zn anode under aqueous conditions, as shown by the equation: $Zn+2H_2O \rightarrow H_2\uparrow+Zn(OH)_2$. Meanwhile, the visualized transparent Zn//Zn symmetric cells are used to observe the reaction phenomena on the surface of zinc foil to analyze the effect of malate additive on the electrolyte/Zn interface HER. As presented in Figure 2m, large amounts of bubble accumulation (H_2), "dead zinc", and dendrites are found on the zinc foil surface with BE. For 50 Mal/BE, under the same conditions, there is neither bubble accumulation nor "dead zinc" on the zinc surface (Figure 2n).

2.5. Zinc Deposition Behavior and Morphology Evolution in Different Electrolytes

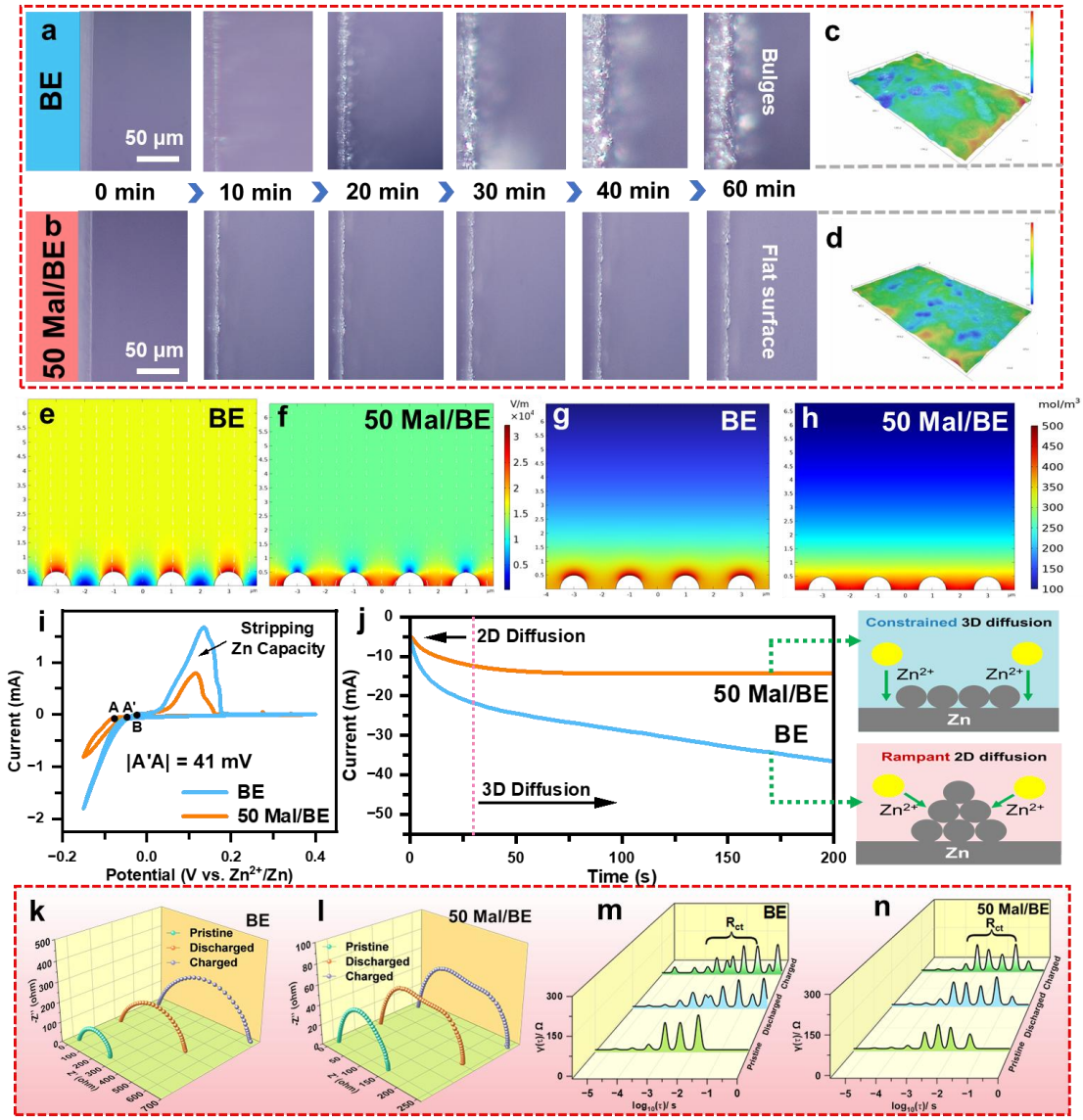

Figure 3. In situ optical microscope observation of the zinc deposition process for the case of (a) BE and (b) 50 Mal/BE, and (c,d) the corresponding optical microscope images after 60 min. The numerical simulation of electric field distribution and equilibrium Zn^{2+} concentration with (e,g) BE and (f,h) 50 Mal/BE. (i) CV curves of the Zn//Cu asymmetric cells with BE and 50 Mal/BE. (j) CA curves of the Zn//Zn symmetric cells with BE and 50 Mal/BE at a constant overpotential of –150 mV and the corresponding schematics of Zn^{2+} diffusion and deposition process. EIS curves of the Zn//Zn symmetric cells with (k) BE and (l) 50 Mal/BE during EIS measurements, and corresponding analysis of distribution of DRT upon galvanostatic in (m) BE and (n) 50 Mal/BE, respectively.

To record the real-time zinc plating courses at different electrolytes, in situ optical microscopy is conducted to monitor the information on zinc anode surface. As presented in Figure 3a, the zinc electrode presents a smooth surface before the electroplating test, and inhomogeneous zinc deposits with preferred nucleation sites is

observed in the BE system after 20 min plating. Further extension of the plating duration causes significant zinc protrusions, which eventually transforms into dendrites with a large size after 60 min. Notably, the appearance of Zn dendrites in BE is accompanied by a large number of bubbles, mainly due to water decomposition throughout the Zn plating process. Conversely, a nearly flat and smooth Zn surface with no visible bubbles and Zn dendrites is found throughout the test in the case of Mal-added electrolyte (Figure 3b). To further confirm the contribution of malate molecules on Zn deposition, 3D optical surface-profilometry images are performed to reveal height difference of electrodes. As depicted in Figure 3c, the Zn surface with BE exhibits a large altitude intercept after 60 min plating due to the rugged surface，while Zn anode with 50 Mal/BE is conspicuously flatter with small altitude intercepts in plating thickness (Figure 3d). To deeply delve into the effect of malate on regulating the interfacial electric field and Zn^{2+} concentration field, the numerical simulation is carried out in the scenario with or without malate additive. As exhibited in Figure 3e, due to the chaotic distribution in electric field and increased intensity on the top of zinc seeds in BE during the process of deposition，Zn^{2+} tends to nucleate around the tips with increased activity, resulting in irregular Zn^{2+} protrusions and random concentrations (Figure 3g). However, the introduction of malate generates uniform electric field in the interface (Figure 3f), thus forcing the high Zn^{2+} concentration to spatially diverge from the electric field and depositing to adjacent flat locations rather than to the tips with lower reactivity and minimum surface energy, ultimately inducing uniform charge redistribution (Figure 3h).

To assess the influence of Mal-regulated EDL structure on zinc deposition behavior, cyclic voltammetry (CV) characterizations of asymmetrical cells in different electrolytes is conducted. The nucleation overpotential (NOP) of the electrolyte is expressed as the interval between A site (reduction potential) and the B site (crossing point). The asymmetric Zn//Cu cell introducing malate additive delivers higher NOP than that BE ($|AA'|$ = 41 mV) (Figure 3i), which may be related to the formation of massive nuclei, leading to fine-grained and compact zinc deposition.[28] Furthermore, the distinct process of zinc deposition in the electrolytes with and without malate

additives can be reflected using chronoamperometry (CA) profiles based on current responses at an overpotential of –150 mV. As schematically depicted in Figure 3j, the Zn electrode in the BE delivers a continuous increase in current density over 200 s, corresponding to uncontrolled 2D diffusion process of Zn^{2+} ions, in which the surface area of the electrode continues to rise arising from the well-known “tip effect”. Unlike that, the tendency towards increasing current density in the 50 Mal/BE is relatively moderate, which could be associated with the dominance of 3D diffusion process during the primary nucleation. In this case, finer nucleus seeds with high areal density are formed at the initial stage, possibly due to the lower barrier in nucleation and rapid growth of (101) crystal plane. During the process of subsequent deposition, 3D diffusion occurs because of the in-plane diffusion deposition process of zinc atoms along the (002) and (100) planes. Distributions of relaxation times (DRT) analysis method is employed to clearly identify the results of in-situ EIS tests for Zn//Zn symmetric batteries (Figures 3k,l). It is reported that peaks ranging from log [τ(s)]; = −1.5～−4 are attributed to the charge transfer process at Zn-ions cross the interface.[29] Expectedly, the charge transfer and ion transport quickly become stable after during the plating/stripping process in 50 Mal/BE, which facilitates transport kinetics of Zn^{2+} and induces uniform Zn deposition (Figures 3m,n). Therefore, it is concluded that malate in HP ameliorates the desolvation of Zn^{2+} and greatly expedites its diffusion kinetics, thus guaranteeing uniform deposition of zinc.

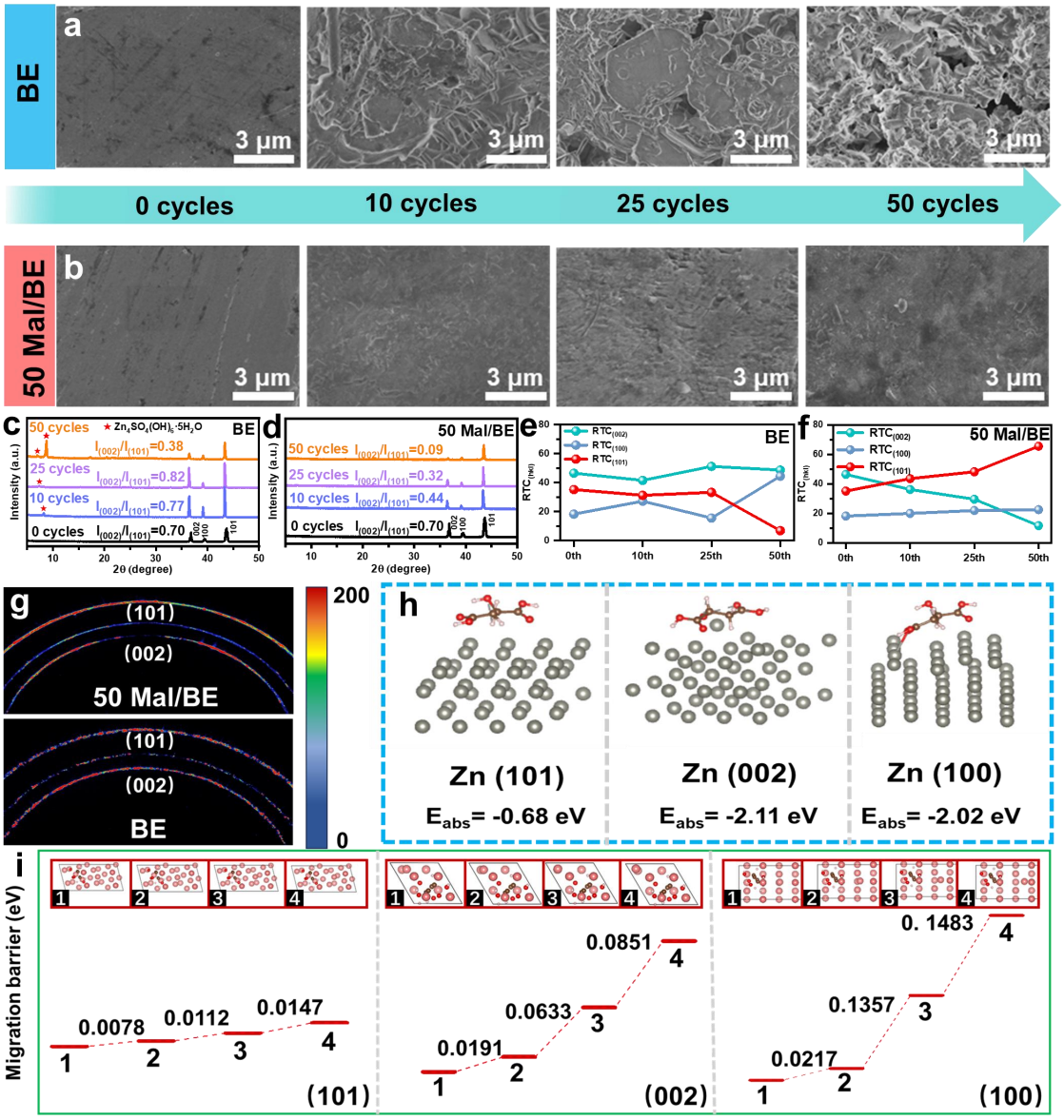

Figure 4. Analysis on the evolution of zinc deposition morphology and crystallographic texture of zinc surface. (a,b) The collected SEM images, and (c,d) XRD patterns of the surface of zinc plate after different cycles in BE and 50 Mal/BE. (e,f) The corresponding line chart for the fitted RTCs of Zn (101), Zn (002), and Zn (100) planes. (g) The 2D GIWAXS results of zinc anodes after 50 cycles in 50 Mal/BE and BE. (h) Adsorption energies of malate molecules on the Zn (101), (002), and (100) facets. (i) Zn^{2+} migration energy on different state Zn surface for malate adsorbed Zn slabs.

In addition to the capability to Zn^{2+} ion migration manipulation, the mechanism behind the significant improvement in electrochemical reversibility empowered by the adsorption layer containing malate is studied via ex situ SEM and XRD analyses. The Zn^{2+} diffusion processes of SEM images in different electrolytes with reasonable morphological evolution after different cycles at 5 mA cm^{-2} with a cutoff capacity of

2.5 mAh cm^{-2} can be schematically described in Figures 4a,b. Obviously, the fresh Zn electrode maintains a smooth and uniform surface, which becomes rather disordered and fragile with the generation of a large number of randomly stacked zinc protrusions after 50 cycles (Figure 4a), and will give rise in serious tip discharge and eventually exacerbates the growth of Zn dendrite in subsequent cycles. The cross-sectional SEM images after 50 cycles shown in Figure S18a, Supporting Information further confirm this process. Instead, the use of 50 Mal/BE enables cycled zinc electrode to possess a compact and dendrite-free deposition with no production of pit and crack throughout the platting/stripping process (Figure 4b and Figure S18b, Supporting Information), consistent well with the excellent improvement in the cycling stability and durability of electrode. Besides, even after 50 cycles, a clean and compact surface with a much smaller fluctuation in height is acquired for the zinc plate from the disassembled battery (Figures S19,20, Supporting Information). Moreover, the thickness of the in post-cycling Zn//Zn symmetric cell with BE shows a continuous increase, in contrast to no significant change in thickness of Zn//Zn with 50 Mal/BE (Figure S21, Supporting Information**)**, which could be due to the effective suppression of parasitic side reactions within the battery by the malate additive during electrochemical cycling. The deposited zinc orientation of different electroplating/stripping cycles in both BE and 50 Mal/BE has been revealed by XRD patterns. In particular, the intensity ratio (R= I_{002}/I_{101}) of (002) and (101) facets are adopted to assess the orientation of zinc platelet deposition. As shown in Figures 4c,d, the R value is 0.70 in Zn foil prior to cycling. Remarkably, the value of R is 0.44 after 10 cycles with malate additive, and then continuously decreases in the following cycles (Figure 4d), which indicates that malate can induce more exposed distinctive Zn (101) texture. In contrast, the value of R changes irregularly with increasing cycles in the BE system (Figure 4c), largely stemming from the random orientation of zinc flakes. For evidencing the textured orientation along (101) in the 50 Mal/BE system, as one of the most crucial indexes, the relative texture coefficient (RTC) for three representative facets of (100), (101), and (002) is further taken into account via the

equation： $RTC_{(hkl)} = \frac{I_{(hkl)}/I_{0(hkl)}}{\sum(I_{(hkl)}/I_{0(hkl)})} \times 100$. [30]A larger value of RCT means that corresponding plane exhibits a higher exposure on the zinc surface.[31] Hence, based on the XRD results, the RTC values of different facets versus cycles of post-cycling Zn foils in different electrolyte systems are further illustrated. As depicted in Figure 4f, Zn (101) plane after adding 50 Mal/BE encounter continuous increment for RTCs as the cycle progresses, whereas a diminished tendency in (002) facet. Specifically, the RTC-value of the Zn (101) plane increases from 35.23 to 65.64, while the value of (002) plane decreases from 46.51 to 11.76. On the contrary, the BE system presents irregular variations after different cycles (Figure 4e), originating from the absence of preferential growth for any zinc planes during the cycling. The comparative analysis of the RTC significantly validates the occurrence of preferred orientation behavior for Zn anode in 50 Mal/BE during cycling, and the manipulation of crystal orientation is achieved by inducing preferential exposure of Zn (101) facet rather than (002) and (100) facets. In addition, the several undesired peaks involving by-product on zinc anode with BE system after cycling can be clearly observed. Different from BE system, the diffraction peaks of are almost absent of cycled Zn anode with the presence of malate additive. The texture and orientation anisotropy of zinc deposition acquired from electrolytes with BE and 50 Mal/BE are also characterized adopting 2D GIWAXS patterns. As evidenced in Figure 4g, the image for zinc deposits acquired from the 50 Mal/BE exhibits a relatively higher Zn (101) peak ratio than that employing BE, which again suggests that Zn (101) becomes the dominant facet of zinc deposits after adding malate.[32]

Based on the properties and atomic arrangement of zinc in various planes of hexagonal close packed (hcp) structure, DFT is employed to calculate the binding energy between different zinc crystal planes of malate. The view of the adsorption mode of malate on each of the Zn (101), (002), and (100) crystal planes and their corresponding values of adsorption energy are exhibited in Figure 4h, respectively. The value for binding affinity with (101) crystal plane (–0.68 eV) is lower than (002) (–2.11 eV) and (100) planes (–2.02 eV), demonstrating that there is less constraint on

Zn^{2+} ions upon (101) facet. The Zn^{2+} ions have a tendency to diffuse to (002) and (100) facets and then deposit, thus, the lowest rate of Zn^{2+} deposition on Zn (101) crystal plane enables Zn (101) texture exposure. The different rates of Zn^{2+} deposition on various crystal planes is further elucidated by Zn^{2+} migration energy. On the malate adsorbed zinc surface, the migration energy of Zn^{2+} under different positions on the Zn (101) is lower than that on Zn (002) and (100) planes (Figure 4i), revealing that the faster migration for Zn ions on Zn (101) facets. In this case, Zn^{2+} ions can easily diffuse along (002) and (100) directions to other facets, boosting distinctive Zn (101) texture exposure, which can be considered as homoepitaxial growth. These results confirm that the malate molecules preferentially adsorb on the zinc surface, controlling zinc deposition rates on different planes and facilitating orientation growth of crystallographic facet.

2.6. Electrochemical Performance Evaluation of Zn Anode

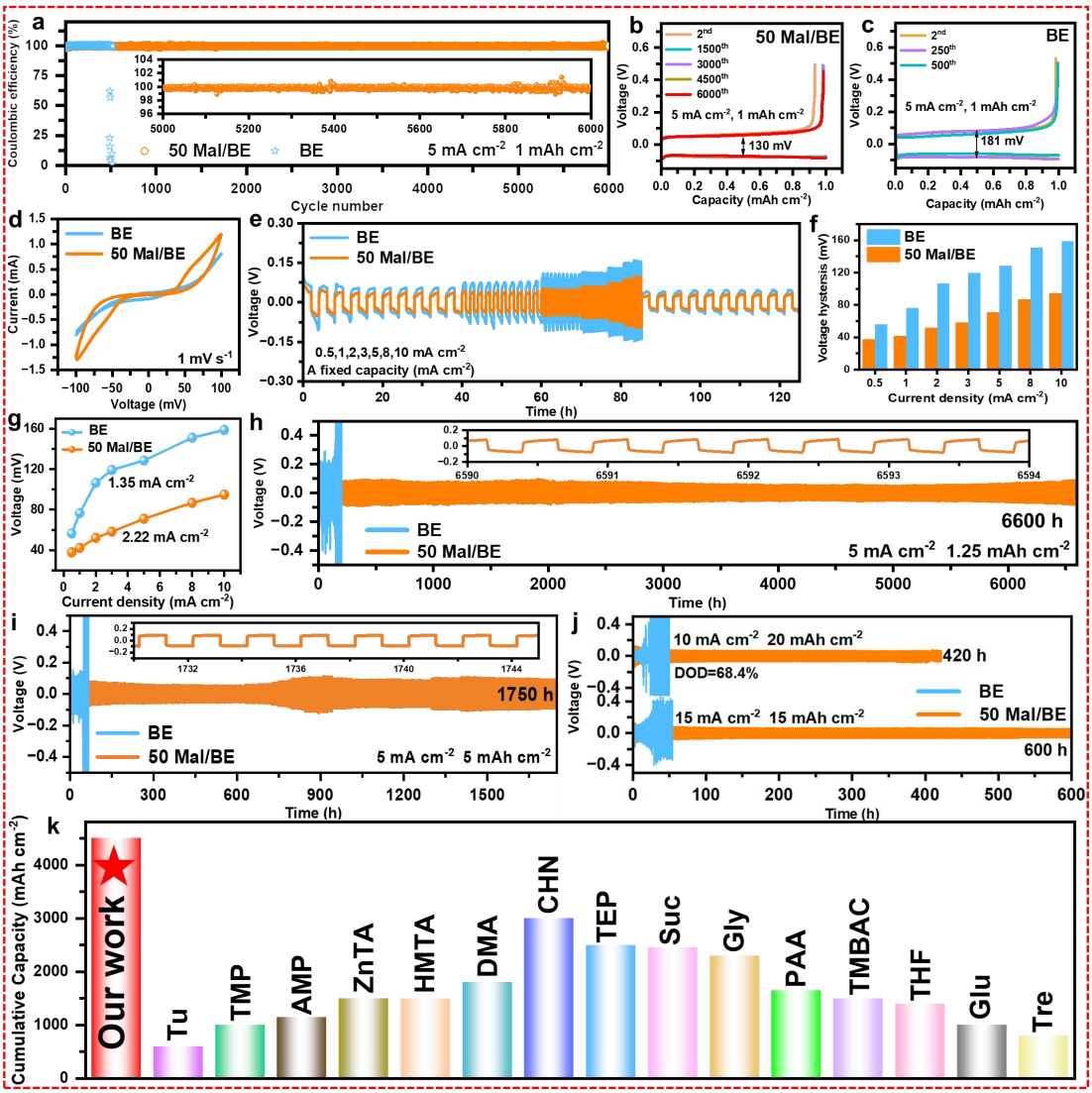

Figure 5. The electrochemical performance of asymmetric and symmetric cells. (a) CE profiles of the asymmetrical cells assembled by different electrodes at 5 mA cm^{-2}/1 mAh cm^{-2}, and the corresponding galvanostatic cycling curves for (b) Zn//Cu cell with 50 Mal/BE and (c) Zn//Cu cell with BE at different cycles. (d) CV profiles of symmetric cells using BE and 50 Mal/BE at 1 mV s^{-1}. (e,f) Rate performance of symmetric cells at current densities from 0.5 to 10 mA cm^{-2} with a fixed capacity of 1 mAh cm^{-2}, and (g) corresponding exchange current densities with BE and 50 Mal/BE. Long-term galvanostatic cycling performance of symmetric cells at current densities/capacities of (h) 5 mA cm^{-2}/1.25 mAh cm^{-2}, (i) 5 mA cm^{-2}/5 mAh cm^{-2} and (j) 10 mA cm^{-2}/20 mAh cm^{-2}, 15 mA cm^{-2}/15 mAh cm^{-2}. (k) Cumulative capacity comparison between this work and recent studies.

Since the nucleation stage is critical to understanding the transition process of zinc dendrites, we compare the nucleation overpotential of zinc in BE and Mal/BE to elucidate how malate molecules regulate the nucleation behavior of zinc. Given these concerns, the nucleation overpotentials of the Zn//Cu asymmetric cells are compared

from the initial voltage profiles of Zn plating at current densities of 1 mA cm^{-2} and 5 mA cm^{-2}. As exhibited in Figure S22, Supporting Information, the nucleation overpotential of Zn electrode in Mal/BE is always lower than that in BE, signifying that the malate-modified EDL can effectively diminish the resistance for zinc nucleation. Interestingly, the asymmetric cell with 50 Mal/BE harvests the optimal performance and is used for the following investigation. The Coulombic efficiency (CE) is also an essential parameter to investigate the influence of malate molecules for reversibility of the Zn plating/stripping during the continuous cycling. Firstly, the Zn//Cu asymmetric cells with/without malate additive are subjected to charge/discharge cycling at the current density of 5 mA cm^{-2} under a capacity of 1 mAh cm^{-2} to evidence the CE, and the results are shown in Figures 5a–c. The Zn//Cu cell in 50 Mal/BE sustains an average CE of ≈ 99.5% over the course of 6000 cycles with stable voltage profiles of only 130 mV. In striking contrast, a significantly short cycling life (≈ 500 cycles), low CE (<98%) and sharp voltage fluctuations (≈181mV) are observed for the Zn//Cu cell adopting BE. When applied to a higher current density of 10 mA cm^{-2} (Figure S23, Supporting Information), the Zn//Cu cell with 50 Mal/BE still shows the smaller voltage hysteresis with a higher average CE of ≈ 99.2% during extended cycle life (over 5000 cycles) compared with the BE system (≈ 96.7%), also indicating that the cycling reversibility can be notably facilitated by the malate additive. The same conclusions can be acquired under a current density of 1 mA cm^{-2} and a current density of 1 mA cm^{-2} (Figure S24, Supporting Information). According to classical thermodynamics, an increase in temperature tends to exacerbate HER. However, even when the Zn//Cu cell with 50 Mal/BE operates at a harsh temperature of 60°C, it still delivers a CE of 98.9% beyond 1500 cycles and steady potential profiles, greatly surpassing that observed in BE (50 cycles, 96.5%) (Figure S25, Supporting Information). The significant enhancement of CE can be ascribed to the favorable effect of malate on adsorption and solvation structure, which blocks side reactions and dendrite formation. To study the reversibility and electrochemical kinetics of symmetric cell with BE and 50 Mal/BE during the plating/stripping process, CV tests are performed at a scan rate of 1 mV s^{-1}. The cell

with 50 Mal/BE possesses a higher maximal current density and larger integrated peak area than BE, underscoring the improved kinetics and interfacial activity for zinc deposition endowed by malate molecules (Figure 5d and Figure S26, Supporting Information). Figures 5e,f reflect the rate capability of symmetric cells in BE and 50 Mal/BE at a cut-off capacity of 1 mAh cm^{-2} and a spectrum of current densities ranging from 0.5 to 10 mA cm^{-2}. Obviously, the symmetric cell in the 50 Mal/BE delivers a distinguished rate performance with substantially lower polarization voltage under all current densities compared to that in BE. To precisely assess the zinc deposition kinetics, the exchange current density (i_0) which is closely related to the zinc electrodeposition process is studied adopting the Butler-Volmer approximation equation： $i = i_0 \frac{2F}{RT} \cdot \eta$.[33] According to the linear fitting, a higher i_0 of 2.22 mA cm^{-2} is acquired for the cell with 50 Mal/BE in contrast to i_0 of 1.35 mA cm^{-2} for the BE (Figure 5g), directly demonstrating that the decreased the overpotential and improved Zn^{2+} transport kinetics due to the presence of malate.

The effect of malate concentration on the electrochemical performance of zinc-symmetric batteries is further investigated. It is found that the long-term galvanostatic cycling stability of 30 Mal/BE and 80 Mal/BE is slightly inferior to that of 50 Mal/BE at the current density of 5 mA cm^{-2} with a fixed areal capacity of 1.25 mAh cm^{-2}, which further emphasizes the necessity of an optimum amount of malate additive. Specifically, the Zn//Zn cell with 50 Mal/BE harvests a an ultralong lifespan (6600 h) approximately 44 times longer than the Zn//Zn cell using BE without the occurrence of obvious fluctuations and presents a low polarization voltage (≈ 84.1 mV) at a current density/capacity of 5 mA cm^{-2}/1.25 mAh cm^{-2} (Figure 5h), indicating a significant improvement in the reversibility of zinc deposition/dissolution. In contrast, the symmetric batteries with 30 Mal/BE and 80 Mal/BE present higher voltage hysteresis after only 650 h and 580 h, respectively (Figure S27, Supporting Information). For one thing, a less concentration of malate is not sufficient to affect the solvent structure, resulting in an inadequate reduction of H_2O activity and the inability to form a solid chemisorption protective layer. For another, an excessive

quantity of malate will cause an increase of Zn nucleation potential (Figure S28, Supporting Information) and the formation of a thicker protective layer on the zinc surface, which leads to a higher energy barrier of zinc deposits and larger charge transfer impedance (Figure S29, Supporting Information). Meanwhile, the battery in the BE system encounters a strong voltage fluctuation, and the polarization voltage abruptly surge after merely ≈150 h, which is a sign of interior short circuit. The poor cycle lifetime and apparent polarization voltage for BE system is ascribed to drastic growth of Zn dendrites and notorious side reactions, which greatly enlarges the interfacial impedance between the Zn foil and the $ZnSO_4$ electrolyte, while the introduction of malate is effective in mitigating the side reactions and dendritic growth of zinc. As a factor affecting zinc deposition, the higher plating/stripping capacity in long-term galvanostatic cycling can increase dendrite size and lead to rampant dendrite formation, thus worsening zinc deposition behavior.[13a] At a high current density/capacity of 5 mA cm^{-2}/5 mAh cm^{-2} (Figure 5i), for BE system, the derived cell merely works for 50 h with sudden and substantial voltage oscillation. With the incorporation of malate molecules, encouragingly, the 50 Mal/BE endows Zn//Zn symmetric cell with an extended lifespan of 1750 h, along with a slightly lower voltage hysteresis of ≈ 94.2 mV, reflecting the diminished energy barrier on the surface of Zn anode in Mal-containing electrolyte for zinc plating/stripping processes.

This stable zinc deposition behavior with 50 Mal/BE is also verified by SEM and XRD after 100 h at 5 mA cm^{-2} (Figure S30, Supporting Information). A loose and messy structure with by-products and dendrites is observed at Zn anode with BE in the SEM, which would lead to intracellular short circuits. On a striking contrast, the Zn electrode still exhibits a highly dense and smooth state after cycling, with no by-products or dendrites in 50 Mal/BE system, which are consistent with XRD results. Also, the S element in the EDS mapping of post-cycling zinc foil with 50 Mal/BE is almost non-existent, while the presence of S element in BE system can be ascribed to the production of by-products (Figure S31, Supporting Information). More impressively, even when adopting a higher current density of 15 mA cm^{-2} at an areal capacity of 15 mAh cm^{-2} (Figure 5j), the 50 Mal/BE system can still ensure stable

zinc plating/stripping operation for about 600 h, much longer than that employing BE. Conversely, the short is witnessed in a very short time (≈22 h) for BE. Take into account that the high depth of discharge (DOD_{Zn} > 40%) is essential to meeting the requirements of practical applications,[34] further interrogation of Zn//Zn cell with malate molecules is performed at a brutal condition of ≈68.4% DOD_{Zn} (current density of 10 mA cm^{-2} and areal capacity of 20 mAh cm^{-2}, Figure 5j). Encouragingly, the Zn//Zn symmetric cells including 50 Mal/BE could sustain highly stable cycling for 420 h, while the ones in BE experiences short circuits with a cycling life of only ca. 30 h, arising from dendrite-induced short-circuit and corrosion. Compared with previously reported works about electrolyte optimization, our work is highly competitive in terms of the cumulative capacity (Figure 5k and Table S2, Supporting Information). The exceptional performance at super-high capacity primarily originates from the fast kinetics caused by facilitating oriented dense deposition of Zn (101) plane. Meanwhile, the ultra-long cycle stability is attributable to the dendrite-free Zn anode composed of flat and smooth Zn (101) texture. Even at a high temperature of 60 °C, malate has shown the ability to stabilize the electrolyte (Figure S32, Supporting Information). Besides, no distinct fluctuation in voltage and overpotential increase are found at voltage-time profiles of the symmetrical cells with 50 Mal/BE after experiencing various standing times from 3 to 15 days (Figure S33, Supporting Information). This can be ascribed to the suppressed competitive HER during the process of cycling, benefitting from the protective layer of adsorbed malate.

2.7. Full Cell Evaluation

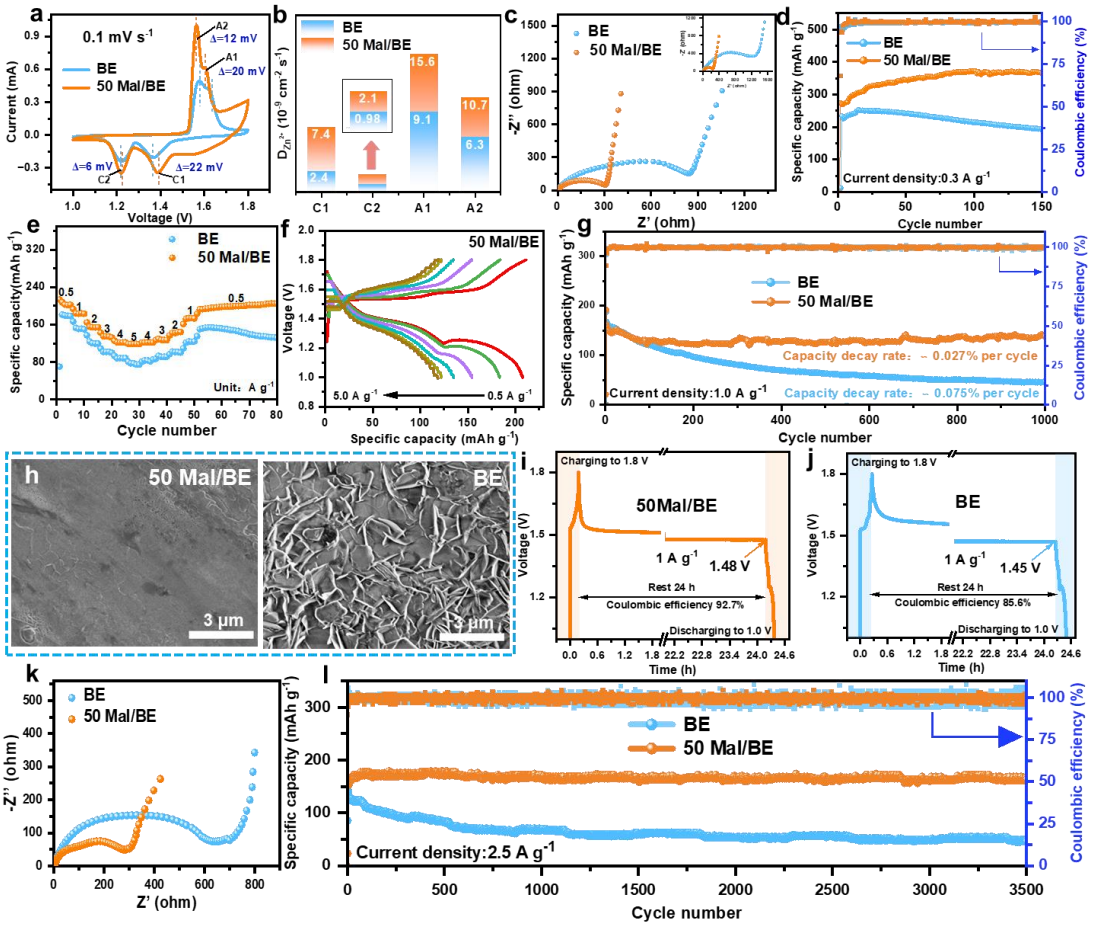

Figure 6. Electrochemical performance of full batteries with BE and 50 Mal/BE. (a) The CV curves of the Zn//MnO_2 cells with the scan rate of 0.1 mV s^{-1}. (b) The D_{Zn}^{2+} values calculated from the CV tests at varied scan rates. (c) EIS plots of the Zn//MnO_2 cells. (d) Cycling performance of Zn//MnO_2 cells at 0.3 A g^{-1}. (e) Rate performance of Zn//MnO_2 cells in at various current density values and (f) corresponding charge/discharge curves. (g) Cycling performance of Zn//MnO_2 cells at 1 A g^{-1}. (h) SEM images of Zn//MnO_2 cells with BE and 50 Mal/BE after 100 cycles at 1 A g^{-1}. Self-discharge test curves of Zn//MnO_2 cells with (i) 50 Mal/BE and (j) BE by resting 24 h. (k) Nyquist plots of the Zn//I_2@CF cells. (l) Long-term cycling performance of Zn//I_2@CF full batteries at 2.5 A g^{-1}.

Ultimately, to further validate the merits of malate in full cells, Zn//α-MnO_2 and Zn//I_2@CF (carbon flowers) full cells are assembled, and their electrochemical properties are investigated. The crystalline structure and morphology characterization of as-synthesized α-MnO_2 and I_2@CF are shown in Figure S34, Supporting Information. The CV profiles of Zn//MnO_2 cells in different electrolytes display two pairs of oxidation and reduction peaks (Figure 6a), which is typical characteristics of α-MnO_2 in $ZnSO_4$ electrolyte. Clearly, the full cell with 50 Mal/BE shows a reduced

voltage polarization in contrast to the BE counterpart, suggesting enhanced charge transfer and facilitated Zn-storage kinetics resulting from the optimized solvation structure by malate. Then, the corresponding Zn^{2+} diffusion coefficients (D_{Zn}^{2+}) values of Zn//MnO_2 full cells are assessed by the CV curves at the scan rate of 0.1–2.0 mV s^{-1},[35] and the fitted slope of peak intensity is presented in Figure S35 and Equation S5, Supporting Information. The D_{Zn}^{2+} of the full-cell employing 50 Mal/BE is larger than that of the BE in all cathodic and anodic reactions (Figure 6b), causing a redistribution in Zn^{2+} flux and makes Zn^{2+} transport faster at the same time.[36] The relationship between the current (i) and sweep rate (v) is as follows: $i(V) = av^b$.[37] In general, when b value is close to 0.5, the main control process is ionic diffusion, while b close to 1 means a capacitive-controlled behavior.[38] The calculated b values of peaks 1–4 are 0.59, 0.71, 0.83, and 0.60, respectively, indicating that the electrochemical kinetics is co-dominated via surface-control and diffusion-control behavior. As illustrated by the Nyquist plots (Figure 6c), the full cell with 50 Mal/BE shows a smaller charge transfer resistance compared to BE, providing evidence that a reduced transport impedance is mainly ascribed to the regulation of the metal-molecule adsorption interface by malate. The full-cell using 50 Mal/BE after 100 cycles still has small electrochemical resistance and large Zn^{2+} ion diffusion compared to that in the BE system without additives.

Subsequently, the cycling performance is evaluated at 0.3 A g^{-1} (Figure 6d). The full cell with 50 Mal/BE can maintain stable discharge capacity during 200 cycles, while BE counterpart shows obvious capacity fading. At a higher current density of 0.5 A g^{-1} (Figure S36, Supporting Information), the Zn//MnO_2 full cell employing the 50 Mal/BE acquires a decent cycling performance at room temperature, with a higher capacity retention after 800 cycles. In contrast, a worse capacity retention occurs in the counterpart utilizing BE, emphasizing the boosted charge transfer and enhanced storage kinetics of Zn owing to the addition of malate. Supportive evidence is also evident in the rate performance, as well as corresponding galvanic charge-discharge (GCD) profiles of full batteries adopting different electrolytes (Figures 6e,f and Figure S37, Supporting Information). As expected, 50 Mal/BE enables MnO_2 cathode

to achieve an outstanding rate performance, with a higher reversible specific capacity of 118.7 mAh g^{-1} at 5 A g^{-1}, exceeding the capacity of BE (≈ 74.5 mAh g^{-1}). Besides, the higher-rate cycling mode of 1 A g^{-1} is employed so as to further illustrate the superiority of Zn//MnO_2 cell with Mal/BE (Figure 6g). The remarkably enhanced discharge capacity of 139.7 mAh g^{-1} at 1 A g^{-1} can be achieved in Zn//MnO_2 battery with 50 Mal/BE after 1000 cycles, corresponding to sluggish capacity loss rate of ca. 0.027% per cycle and a stable CE of nearly 100%, superior to that of the full-battery with BE, with reversible capacity of 46.4 mAh g^{-1} at 1 A g^{-1} (capacity decay rate: ≈ 0.075% per cycle). The corresponding 3D optical microscope images presents a coarser distributed surface with a larger maximum height difference for the cell with BE after cycling, while relatively flat surface with a low altitude intercept is observed for post-cycling cell with 50 Mal/BE (Figure S38, Supporting Information). The SEM images of Zn//MnO_2 cells after cycling further explain detailed illustration. As shown in Figure 6h and Figures S38–41, Supporting Information, the zinc anode with BE exhibits an extremely rough surface with a large number of rampant dendrites, increasing the risk of battery failure. In contrast, the anode with Mal-adding electrolyte maintains an intact and smooth surface after cycling. Similar conclusion of the benefits with the presence of malate additive could be also witnessed XRD patterns (Figure S42, Supporting Information). The self-discharge phenomenon of the fully charged cells is then detected to assess the storage performance of aqueous battery system during shelf life (Figures 6i,j). After resting for 24 h, the Zn//MnO_2 battery with 50 Mal/BE maintains a high-capacity retention of 92.7% of its original capacity due to the suppressed parasitic reactions, far outperforming the BE case (85.6% retention), underscoring the ability of malate to restrain by-product generation. To further affirm the advantageous nature of our investigated electrolyte system, we have conducted a series of tests to estimate the performance Zn//MnO_2 full cells under higher load conditions of 2.1 mg cm^{-2}. The long-term cycling stability at the higher cathode load is investigated at a current density of 1 A g^{-1} as exhibited in Figure S43, Supporting Information. The cell with 50 Mal/BE still yields a reversible specific capacity of 107.1 mAh g^{-1} after 1000 cycles, corresponding to a retention of 63%

compared with the capacity decays rapidly and fails only 170 cycles for BE system. It suggested that 50 Mal/BE can suppress the structure deterioration of MnO_2 cathode at high-loading conditions.

In addition to α-MnO_2 cathode, I_2@CF cathode is employed to match with Zn anode, constructing full cells. As shown in Figure S44, Supporting Information, the CV curves show that similar redox potentials in both electrolytes, and the reversibility of the voltage of Zn//I_2@CF cell in 50 Mal/BE is more stable. This result is further demonstrated by the R_{ct} values acquired from the EIS curves of the Zn//I_2@CF full cells. As presented in the Nyquist plots at the initial state (Figure 6k), the R_{ct} of Zn//I_2@CF cell with 50 Mal/BE is much lower than that of the BE and indicative of nominal polarization and quick Zn^{2+} transfer. When the current density is 2.5 A g^{-1}, the AZIB including 50 Mal/BE possesses a high discharge specific capacity of 91.0% of the initial capacity, while the AZIB with BE only maintains 31.5% after 3500 cycles (Figure 6l). All the above results confirm the success of achieving highly reversible zinc anodes by adopting 50 mM malate to customize the zinc/electrolyte interface with a moderate degree of H_2O-poor EDL, as well as achieve ordered Zn (101) crystallographic orientation of AZIBs.

2.8. Hydrogel Electrolytes Evaluation

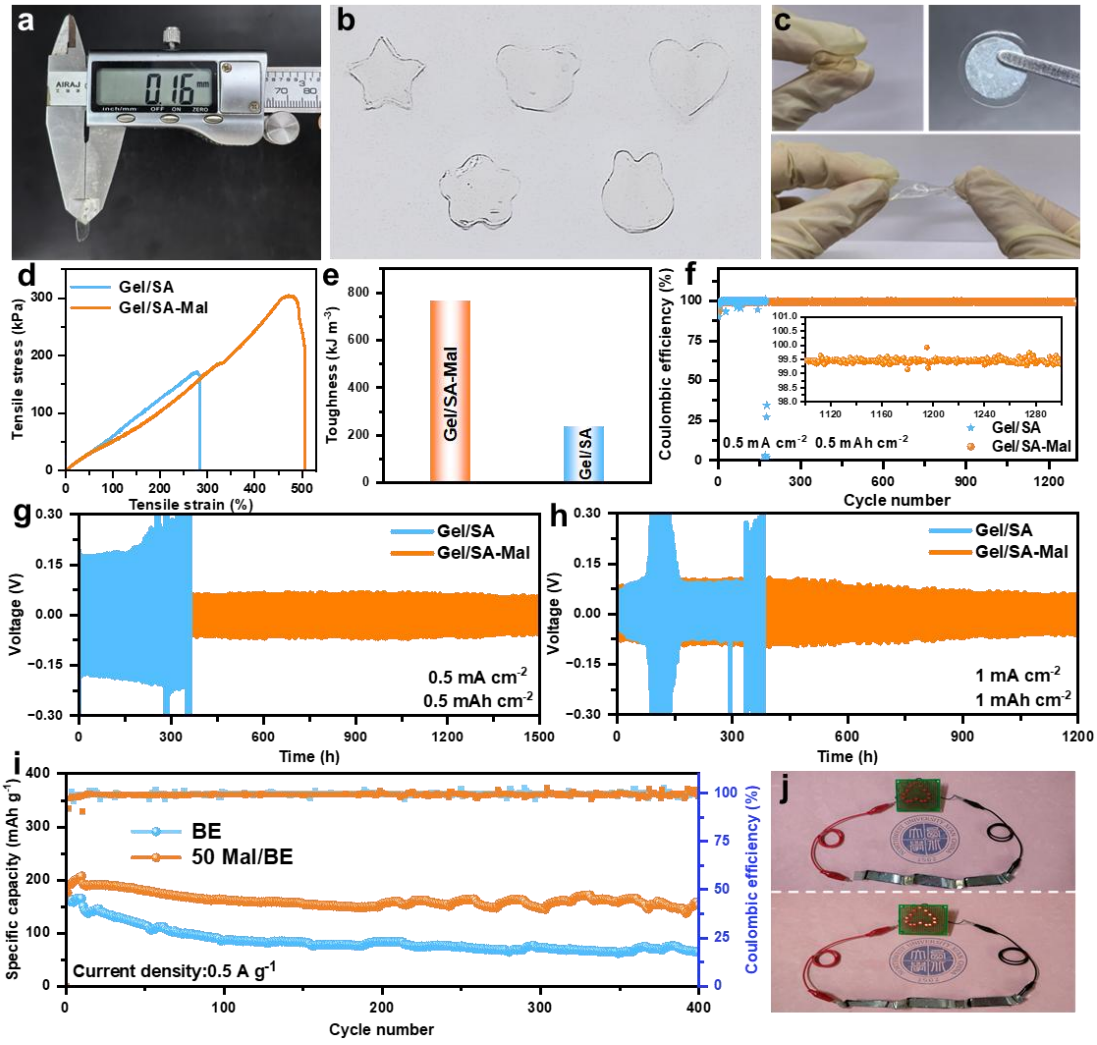

Figure 7. (a) Optical photograph of the thickness measured with a micrometer of dried Gel/SA-Mal. (b) Gel/SA-Mal molded in various patterns. (c) Digital images of Gel/SA-Mal under different deformations of bending, twisting and interface adhesion between Gel/SA-Mal and Zn substrates. (d) Tensile stress-strain profiles and (e) toughness comparison of Gel/SA and Gel/SA-Mal. (f) CE of Zn//Cu cells in Gel/SA and Gel/SA-Mal at 0.5 mA cm^{-2}/0.5 mAh cm^{-2}. Zn plating/stripping profiles of Zn//Zn symmetric cells in Gel/SA and Gel/SA-Mal at respective current density and capacity values of (g) 0.5 mA cm^{-2} and 0.5 mAh cm^{-2}, and (h) 1 mA cm^{-2} and 1 mAh cm^{-2}. (i) Cycling performance of Zn//MnO_2 full batteries in Gel/SA and Gel/SA-Mal at 0.5 A g^{-1}. (j) Photograph of LED display powered by three charged Zn//MnO_2 cells in series.

Compared with liquid electrolyte, gel electrolytes possess higher ion conductivity and safer performance towards AZIBs. In particular, gels with groups in the molecular chain can significantly promote ion migration, resulting in higher ionic conductivity and transference number. Besides, the gel polymer electrolyte has a low water content, as well as cross-linked network structure, which limits the free diffusion of H_2O

molecules, and in some cases can restrain dendrite growth and HER in the anode.[39] Inspired by abovementioned results, we designed an innovative double-network hydrogel electrolyte with a thickness of ≈ 0.16 mm to deal with issues faced by zinc anodes (Figure 7a), consisting of gelatin (Gel), sodium alginate (SA), malate and $ZnSO_4$ (denoted as Gel/SA-Mal). Mechanical performances are essential evaluation criteria when employing quasi-solid-state electrolytes in energy storage systems, which directly reflect the adaptability to external stress and deformations. According to its unique chemical structures, the as-synthesized hybrid hydrogel electrolyte can be designed into arbitrary shapes without any damage at various mechanical manipulation under ambient temperature, including bending and twisting (Figures 7b,c). Moreover, the adhesive properties play a vital role for hydrogel-based electronics to develop a strong interfacial connection between electrodes and electrolytes. The experiment is conducted for such hydrogel on Zn substrate to determine the strength in adhesion. As demonstrated in Figure 7c, Gel/SA-Mal exhibits good adhesion to zinc sheet due to the coordination effect from –COOH and –OH groups. In addition, tensile tests are employed to quantitatively study the mechanical properties. After the addition of SA and malate, the tensile stress of Gel/SA-Mal under 505% strain is 305.7 kPa (Figure 7d), whereas the corresponding value of Gel/SA is merely 171.5 kPa under 170% strain. Accordingly, the toughness of Gel/SA-Mal reaches 764.1 kJ m^{-3} (Figure 7e), which is also markedly higher than that of Gel/SA (239.4 kJ m^{-3}). The substantial increment in the mechanical strength of the Gel/SA-Mal hydrogel is primarily due to the improved inter-chain electrostatic attraction and the reconstruction of hydrogen bond networks caused by –COOH and –OH components, which has facilitated the advancement of hybrid polymer systems for excellent strength and adaptability. Interestingly, as shown in Figure S45, Supporting Information, the Gel/SA-Mal harvests a higher ionic conductivity of 37.3 mS cm^{-1} calculated from the Nyquist plot compared to that of Gel/SA (24.4 mS cm^{-1}), superior to the most of present research on gel electrolytes (Table S3, Supporting Information).

To confirm the advantages of Gel/SA-Mal adaptability on zinc metal anode, it is

essential to evaluate the CE to measure the stable reversibility of Zn plating/stripping in Zn//Cu asymmetric cells system. As depicted in Figure 7f, the asymmetrical cell including Gel/SA-Mal can provide a CE of 99.5% after 1300 cycles at the current density/areal capacity of 0.5 mA cm^{-2}/0.5 mAh cm^{-2}. On the contrary, the cell including Gel/SA can only run for less than 170 cycles before suddenly dropping to less than 40% in a few cycles. Figure 7g exhibits that the voltage profiles at different cycles for Gel/SA-Mal possesses lower voltage hysteresis than that for Gel/SA, suggesting that a lower energy barrier for zinc nucleation/dissolution in the Gel/SA-Mal system. Moreover, it has proven to harvest an elongated lifespan, operating for 1500 h at a current density of 0.5 mA cm^{-2} and 0.5 mAh cm^{-2} capacity. Meanwhile, the symmetric cell with Gel/SA presents obvious fluctuations in potential after plating/stripping performance of ≈ 200 h. Furthermore, the impressive durable performance of Zn//Zn deposition/dissolution is acquired for Gel/SA-Mal under a larger current density. At 1 mA cm^{-2} with a limited capacity of 1 mAh cm^{-2} (Figure 7h), stripping/plating cycling performance in the Gel/SA-Mal system beyond 1200 h is observed, while the poor cyclability of Zn//Zn symmetric cell with Gel/SA is exhibited after merely 70 h. To investigate the practicality of the design of hydrogel electrolyte, the Zn//MnO_2 battery is assembled using Gel/SA and Gel/SA-Mal. Intriguingly, at 0.5 A g^{-1}, the full cell with Gel/SA-Mal operates at extended calendar life, and apparently establishes a significant stable performance of 400 cycles and 89.8% capacity retention (Figure 7i). By comparison, the battery including Gel/SA demonstrates unsatisfactory cycling performance, rapid loss for capacity, and failed operation. As presented in Figure 7j, the red LED light can be lightened by the Zn//MnO_2 battery with Gel/SA-Mal system, indicating its successful practical application. The superior cycling stability of the cells can be ascribed to the Gel/SA-Mal with high ionic conductivity and mechanical features, which can ensure uniform and stable Zn electrode/electrolyte interface, suppress Zn dendrite growth, and induce dendrite-free zinc deposition.

3.Conclusion

In summary, this study comprehensively reveals that the significant improvements in the performance of AZIBs facilitated by addition of malate into the $ZnSO_4$ electrolyte. Our investigation has highlighted the key role played by the –COOH and –OH functional groups present in the molecular additives, explicating their profound influence on adsorption mechanisms, electric double layer regulation, as well as solvation structure of Zn^{2+}. Remarkably, functional groups such as –COOH and –OH harvest strong interactions with zinc metal surface, promoting preferential adsorption and chelation with Zn^{2+} ions. Also, the adsorbed malate boosts the exposure of unconventional (101) crystal plane for dendrite-free zinc anodes. It is exciting that the tactics enables the Zn//Zn symmetric cell to stably work for 6600 h at 5 mA cm^{-2}/1.25 mAh cm^{-2}. The cell with a DOD of 68.4% is achieved in 50 Mal/BE even under demanding test conditions of 10 mA cm^{-2} and 20 mAh cm^{-2}, corresponding to an ultra-high cumulative capacity of 4.2 Ah cm^{-2}, way better than the state-of-art zinc anodes. Additionally, the assembled Zn//MnO_2 full cell delivers improved cycling performance of more than 1000 stable cycles with sluggish capacity loss rate of 0.027% per cycle. More intriguingly, the as-prepared Gel/SA-Mal system can effectively facilitate stability in symmetric cells (1200 h at 1 mA cm^{-2}/1 mA cm^{-2}) and boost the reversibility of Zn plating-stripping in Zn//Cu asymmetric cells system (average CE of 99.5%). This work contributes to the advancement of emerging Zn chemistries and hold promise for the development of more reliable solutions in energy storage systems.

Additional information

Supporting Information accompanies this paper in the online version of the paper.

Acknowledgements

This work was supported by the National Natural Science Foundation of China (No. 22075227) and Shaanxi Fundamental Science Research Project for Chemistry and Biology (Grant No. 23JHQ011).

Conflict of interest

There is no conflict to declare.

Data Availability Statement

The data that support the findings of this study are available from the corresponding author upon reasonable request.

References

[1] a) M. Shi, T. Sun, W. Zhang, Q. Nian, Q. Sun, M. Cheng, J. Liang, Z. Tao, *Angew. Chem., Int. Ed.* **2024**, n/a, e202407659; b) F. Wang, O. Borodin, T. Gao, X. Fan, W. Sun, F. Han, A. Faraone, J. A. Dura, K. Xu, C. Wang, *Nat. Mater.* **2018**, 17, 543; c) Q. Li, A. Chen, D. Wang, Z. Pei, C. Zhi, *Joule* **2022**, 6, 273.

[2] a) J. Cao, H. Wu, D. Zhang, D. Luo, L. Zhang, X. Yang, J. Qin, G. He, *Angew. Chem., Int. Ed.* **2024**, 63, e202319661; b) S. Wang, Z. Huang, J. Zhu, Y. Wang, D. Li, Z. Wei, H. Hong, D. Zhang, Q. Xiong, S. Li, Z. Chen, N. Li, C. Zhi, *Adv. Mater.* **2024**, n/a, 2406451.

[3] J. Lu, T. Wang, J. Yang, X. Shen, H. Pang, B. Sun, G. Wang, C. Wang, *Angew. Chem., Int. Ed.* **2024**, n/a, e202409838.

[4] X. Fan, H. Yang, X. Wang, J. Han, Y. Wu, L. Gou, D.-L. Li, Y.-L. Ding, *Advanced Materials Interfaces* **2021**, 8, 2002184.

[5] Y. Wang, T. Ren, Z. Wang, C. Liu, Y. Zhang, A. Xu, C. Chen, J. Bai, H. Wang, X. Liu, *Adv. Energy Mater.* **2024**, 14, 2400613.

[6] X. Yang, W. Li, Z. Chen, M. Tian, J. Peng, J. Luo, Y. Su, Y. Zou, G. Weng, Y. Shao, S. Dou, J. Sun, *Angew. Chem., Int. Ed.* **2023**, 62, e202218454.

[7] a) G. Wang, Q.-K. Zhang, X.-Q. Zhang, J. Lu, C. Pei, D. Min, J.-Q. Huang, H. S. Park, *Adv. Energy Mater.* **2024**, n/a, 2304557; b) Y. Yang, Y. Li, Q. Zhu, B. Xu, *Adv. Funct. Mater.* **2024**, n/a, 2316371.

[8] K. Qi, P. Liang, S. Wei, H. Ao, X. Ding, S. Chen, Z. Fan, C. Wang, L. Song, X. Wu, C. Wu, Y. Zhu, *Energy Environ. Sci.* **2024**, 17, 2566.

[9] N. Hu, W. Lv, W. Chen, H. Tang, X. Zhang, H. Qin, D. Huang, J. Zhu, Z. Chen, J. Xu, H. He, *Adv. Funct. Mater.* **2024**, 34, 2311773.

[10] J. Luo, L. Xu, Y. Zhou, T. Yan, Y. Shao, D. Yang, L. Zhang, Z. Xia, T. Wang, L. Zhang, T. Cheng, Y. Shao, *Angew. Chem., Int. Ed.* **2023**, 62, e202302302.

[11] S. jiao, J. Fu, Q. Yin, H. Yao, H. Hu, *Energy Storage Mater.* **2023**, 59, 102774.

[12] Z. Zhao, R. Wang, C. Peng, W. Chen, T. Wu, B. Hu, W. Weng, Y. Yao, J. Zeng, Z. Chen, P. Liu, Y. Liu, G. Li, J. Guo, H. Lu, Z. Guo, *Nat. Commun.* **2021**, 12, 6606.

[13] a) Y. Wang, Z. Deng, B. Luo, G. Duan, S. Zheng, L. Sun, Z. Ye, J. Lu, J. Huang, Y. Lu, *Adv. Funct. Mater.* **2022**, 32, 2209028; b) G. Ma, W. Yuan, X. Li, T. Bi, L. Niu, Y. Wang, M. Liu, Y.

Wang, Z. Shen, N. Zhang, *Adv. Mater.* **2024**, n/a, 2408287.

[14] a) Y. Wang, L. e. Mo, X. Zhang, Y. Ren, T. Wei, Z. Li, Y. Huang, H. Zhang, G. Cao, L. Hu, *Adv. Energy Mater.* **2023**, 13, 2301517; b) Y. Zou, X. Yang, L. Shen, Y. Su, Z. Chen, X. Gao, J. Zhou, J. Sun, *Energy Environ. Sci.* **2022**, 15, 5017.

[15] Z. Liu, Z. Guo, L. Fan, C. Zhao, A. Chen, M. Wang, M. Li, X. Lu, J. Zhang, Y. Zhang, N. Zhang, *Adv. Mater.* **2024**, 36, 2305988.

[16] Z. Cheng, K. Wang, J. Fu, F. Mo, P. Lu, J. Gao, D. Ho, B. Li, H. Hu, *Adv. Energy Mater.* **2024**, 14, 2304003.

[17] M. Shi, C. Lei, H. Wang, P. Jiang, C. Xu, W. Yang, X. He, X. Liang, *Angew. Chem., Int. Ed.* **2024**, n/a, e202407261.

[18] D. Wang, D. Lv, H. Liu, S. Zhang, C. Wang, C. Wang, J. Yang, Y. Qian, *Angew. Chem., Int. Ed.* **2022**, 61, e202212839.

[19] Y. Lv, M. Zhao, Y. Du, Y. Kang, Y. Xiao, S. Chen, *Energy Environ. Sci.* **2022**, 15, 4748.

[20] X. Huo, Z. Zhou, W. Huang, G. Gao, B. Li, J. Bi, Z. Du, W. Ai, *Energy Environ. Sci.* **2024**.

[21] H. Qin, W. Kuang, D. Huang, X. Zhang, J. Liu, L. Yi, F. Shen, Z. Wei, Y. Huang, J. Xu, H. He, *J. Mater. Chem. A* **2022**, 10, 17440.

[22] H. Wang, W. Ye, B. Yin, K. Wang, M. S. Riaz, B.-B. Xie, Y. Zhong, Y. Hu, *Angew. Chem., Int. Ed.* **2023**, 62, e202218872.

[23] S. Zhou, X. Meng, Y. Chen, J. Li, S. Lin, C. Han, X. Ji, Z. Chang, A. Pan, *Angew. Chem., Int. Ed.* **2024**, 63, e202403050.

[24] H. Liu, J.-G. Wang, W. Hua, L. Ren, H. Sun, Z. Hou, Y. Huyan, Y. Cao, C. Wei, F. Kang, *Energy Environ. Sci.* **2022**, 15, 1872.

[25] W. Zhang, F. Guo, H. Mi, Z.-S. Wu, C. Ji, C. Yang, J. Qiu, *Adv. Energy Mater.* **2022**, 12, 2202219.

[26] M. Qiu, P. Sun, Y. Wang, L. Ma, C. Zhi, W. Mai, *Angew. Chem., Int. Ed.* **2022**, 61, e202210979.

[27] H. Liu, Z. Xin, B. Cao, Z. Xu, B. Xu, Q. Zhu, J.-L. Yang, B. Zhang, H. J. Fan, *Adv. Funct. Mater.* **2024**, 34, 2309840.

[28] H. Qin, W. Chen, W. Kuang, N. Hu, X. Zhang, H. Weng, H. Tang, D. Huang, J. Xu, H. He, *Small* **2023**, 19, 2300130.

[29] a) M. Yan, C. Xu, Y. Sun, H. Pan, H. Li, *Nano Energy* **2021**, 82, 105739; b) H. Li, Y. Ren, Y. Zhu, J. Tian, X. Sun, C. Sheng, P. He, S. Guo, H. Zhou, *Angew. Chem., Int. Ed.* **2023**, 62, e202310143.

[30] M. Zhou, S. Guo, J. Li, X. Luo, Z. Liu, T. Zhang, X. Cao, M. Long, B. Lu, A. Pan, G. Fang, J. Zhou, S. Liang, *Adv. Mater.* **2021**, 33, 2100187.

[31] W. Yuan, X. Nie, G. Ma, M. Liu, Y. Wang, S. Shen, N. Zhang, *Angew. Chem., Int. Ed.* **2023**, 62, e202218386.

[32] Y. Su, B. Chen, Y. Sun, Z. Xue, Y. Zou, D. Yang, L. Sun, X. Yang, C. Li, Y. Yang, X. Song, W. Guo, S. Dou, D. Chao, Z. Liu, J. Sun, *Adv. Mater.* **2023**, 35, 2301410.

[33] J. B. Park, C. Choi, J. H. Park, S. Yu, D.-W. Kim, *Adv. Energy Mater.* **2022**, 12, 2202937.

[34] X. Shi, J. Wang, F. Yang, X. Liu, Y. Yu, X. Lu, *Adv. Funct. Mater.* **2023**, 33, 2211917.

[35] N. Zhang, M. Jia, Y. Dong, Y. Wang, J. Xu, Y. Liu, L. Jiao, F. Cheng, *Adv. Funct. Mater.* **2019**, 29, 1807331.

[36] J. B. Park, C. Choi, S. W. Jung, B. C. Min, J. H. Park, D.-W. Kim, *Adv. Mater.* **2024**, 36, 2308684.

[37] Y. Zhang, T. Ren, C. Liu, Q. Wu, Y. Xia, X. Liu, *Small* **2024**, n/a, 2401789.

[38] a) H. Li, Z. Wang, L. Dang, K. Yu, R. Yang, A. Fu, X. Liu, Y.-G. Guo, H. Li, *Small* **2024**, 20, 2307722; b) H. Li, Z. Wang, L. Dang, K. Yu, R. Yang, A. Fu, X. Liu, Y.-G. Guo, H. Li, X. S. Zhao, *Energy Storage Mater.* **2024**, 70, 103547.

[39] J. Kumankuma-Sarpong, C. Chang, J. Hao, T. Li, X. Deng, C. Han, B. Li, *Adv. Mater.* **2024**, 36, 2403214.